**Atmospheric
Measurement
Techniques
Discussions**

Retrieval of tropospheric NO_2 using the MAX-DOAS method combined with relative intensity measurements for aerosol correction

T. Vlemmix[1,2], A. J. M. Piters[1], P. Stammes[1], P. Wang[1], and P. F. Levelt[1,2]

[1]Royal Netherlands Meteorological Institute, KNMI, The Netherlands
[2]Eindhoven University of Technology, The Netherlands

Correspondence to: T. Vlemmix (vlemmix@knmi.nl)

Discussion Paper | Discussion Paper | Discussion Paper | Discussion Paper

AMTD

3, 2317–2366, 2010

MAX-DOAS aerosol corrected tropospheric NO_2 columns

T. Vlemmix et al.

Title Page

Abstract	Introduction
Conclusions	References
Tables	Figures

|◀ | ▶|
◀ | ▶

Back | Close

Full Screen / Esc

Printer-friendly Version

Interactive Discussion

T. Vlemmix et al.

Title Page

Abstract | Introduction

Conclusions | References

Tables | Figures

◀ | ▶|

◀ | ▶

Back | Close

Full Screen / Esc

Printer-friendly Version

Interactive Discussion

Abstract

Multi-Axis Differential Optical Absorption Spectroscopy (MAX-DOAS) is a technique to measure trace gas amounts in the lower troposphere from ground-based scattered sunlight observations. MAX-DOAS observations are especially suitable for validation of tropospheric trace gas observations from satellite, since they have a representative range of several kilometers, both in the horizontal and in the vertical dimension.

A two-step retrieval scheme is presented here, to derive aerosol corrected tropospheric NO$_2$ columns from MAX-DOAS observations. In a first step, boundary layer aerosols, characterized in terms of aerosol optical thickness (AOT), are estimated from relative intensity observations, which are defined as the ratio of the sky radiance at elevation α and the sky radiance in the zenith. Relative intensity measurements have the advantage of a strong dependence on boundary layer AOT and almost no dependence on boundary layer height. In a second step, tropospheric NO$_2$ columns are derived from differential slant columns, based on AOT-dependent air mass factors.

This two-step retrieval scheme was applied to cloud free periods in a twelve month data set of observations in De Bilt, the Netherlands. In a comparison with AERONET (Cabauw site) a mean difference in AOT (AERONET minus MAX-DOAS) of −0.01±0.08 was found, and a correlation of 0.85. Tropospheric-NO$_2$ columns were compared with OMI-satellite tropospheric NO$_2$. For ground-based observations restricted to uncertainties below 10%, no significant difference was found, and a correlation of 0.88.

1 Introduction

1.1 Validation of satellite NO$_2$ data

Tropospheric nitrogen dioxide (NO$_2$) plays an important role in atmospheric chemistry. It is involved in many chemical cycles such as in the formation of tropospheric ozone,

which is toxic to humans. High concentrations of NO_2 often indicate high levels of air pollution in general.

The trace gas NO_2 is monitored in various ways. Primarily by surface in-situ monitoring stations all over the world, but since the last decade also from space. Space borne observations of NO_2 form the basis for studies of regional and global trends, global transport and chemical cycles (e.g. Richter et al., 2005; van der A et al., 2006; Blond et al., 2007, and Boersma et al., 2008). In addition, satellite observations of tropospheric NO_2 are essential for validation of atmospheric chemical transport models and top-down construction of emission data bases (e.g. Martin et al., 2003; Mijling et al., 2009).

Despite the many results of observations from space, there is still a great demand for independent, quantitative validation of the NO_2 retrievals (Brinksma et al., 2008; Irie et al., 2008b; Hains et al., 2010). Validation should be performed under various atmospheric conditions and in different parts of the world, since it is known that clouds, aerosols, surface albedo, surface altitude, trace gas profile and other parameters all have significant impact on the satellite retrievals (e.g. Boersma et al., 2004; Zhou et al., 2009).

Whereas satellite validation of ozone retrievals is often done by comparison with ozone-sondes, there is not yet an equivalent in-situ profiling measurement for NO_2. Comparing to in-situ surface monitors is problematic due to the large difference in spatial representativeness of the two observation techniques: In-situ surface monitors have a local character (e.g. street level), whereas even the smallest pixels of current trace gas monitoring satellite instruments have sizes of several hundreds of square kilometers. Although rural stations are representative for larger regions (Blond et al., 2007), comparison with satellite observations requires strong assumptions on the vertical distribution of NO_2.

1.2 MAX-DOAS method

The Multi-Axis Differential Optical Absorption Spectroscopy (MAX-DOAS) method (e.g. Wagner et al., 2004; Hönninger et al., 2004; Wittrock et al., 2004; Sinreich et al., 2005; Friess et al., 2006; Leigh et al., 2007; Irie et al., 2008a) offers an alternative in this respect, since it has a much larger spatial representativeness than in-situ surface monitors. MAX-DOAS instruments observe scattered solar radiation from the surface – in the UV and/or Visible – at a spectral resolution of typically 0.5 nm in multiple viewing directions (see Fig. 1). Small elevations have a relatively high sensitivity to the lower troposphere, since detected photons at small elevations have longer paths through these layers than photons observed at larger elevations. Radiative transfer simulations show that the horizontal representative range is about 5 to 10 km, whereas the vertical range is about 1 to 4 km. Both the horizontal and vertical range have a strong dependence on elevation, see e.g. Wittrock et al. (2004) and Pikelnaya et al. (2007). The increased sensitivity to the lower troposphere also distinguishes the MAX-DOAS technique from other ground-based passive DOAS techniques, such as direct-sun DOAS (total column NO_2, see e.g. Herman et al., 2009), and zenith sky DOAS (stratospheric NO_2, see e.g. Melo et al., 2005).

The various DOAS techniques (see Platt and Stutz, 2008, for an extensive overview) have in common that the analysis of spectral measurements of atmospheric radiation is based on the DOAS equation:

$$\ln\left(\frac{I(\lambda)}{I_{\text{ref}}(\lambda)}\right) = -\sum_{i=1}^{n}\Delta\sigma_i(\lambda)\Delta N_i^S + P(\lambda). \tag{1}$$

In this equation n differential cross-section spectra $\Delta\sigma(\lambda)_{i=1,n}$ and a low-order polynomial $P(\lambda)$ are fitted to the natural logarithm of the ratio of two atmospheric spectra $I(\lambda)$. A differential cross-section uniquely characterizes a trace gas and is obtained by subtracting a low-order polynomial from the cross-section. The two atmospheric spectra in the DOAS equation correspond to two different viewing directions, or times of

observation, or both, depending on the specific DOAS application.

The fitting procedure yields a so-called differential slant column (density) ΔN^S in [molecules/cm^2] for each trace gas. The differential slant column represents the difference in trace gas absorption along the two light paths corresponding to the atmospheric spectra. In the case of MAX-DOAS, it is custom to combine a zenith spectrum with a spectrum corresponding to another, preferably small, elevation α, since photons detected at small elevation have the largest path length difference with photons detected in the zenith, and this combination thus gives a high sensitivity to the lower troposphere.

In this study, MAX-DOAS observations are used for the retrieval of tropospheric columns of NO$_2$. To convert a differential slant column to a corresponding tropospheric vertical column N^{Tr}, a so called differential air mass factor ΔM is required. This factor is a function of the elevation α – and to a lesser extent of many other parameters – and is defined here as the ratio of the differential slant column density and the tropospheric column density of NO$_2$:

$$\Delta M_\alpha = \frac{\Delta N^S_\alpha}{N^{Tr}}. \tag{2}$$

The simplest calculation of MAX-DOAS differential air mass factors has become known as the geometrical approximation (Hönninger et al., 2004). The geometrical approximation is not based on radiative transfer simulations, but assumes that the last scattering altitude of photons detected at the surface is below the stratosphere and above the tropospheric layer of a trace gas. This assumption leads to the following relation:

$$\Delta M_\alpha = \frac{1 - \sin(\alpha)}{\sin(\alpha)}. \tag{3}$$

Although the geometrical approximation is known to be inaccurate for small elevations (see e.g. Wittrock et al., 2004; Pinardi et al., 2008), this approximation is believed to give an acceptable first estimate of the tropospheric column if applied to a relatively

Title Page

Abstract | Introduction

Conclusions | References

Tables | Figures

|◄ | ►|

◄ | ►

Back | Close

Full Screen / Esc

Printer-friendly Version

Interactive Discussion

large elevation, such as 30°. The geometrical approximation is used in e.g. Brinksma et al. (2008), Hains et al. (2010) and Wagner et al. (2010).

To exploit the high sensitivity of the MAX-DOAS technique at small elevations, it is desirable to have appropriate differential air mass factors for these viewing directions. This requires a more sophisticated description of the radiative transfer than the geometrical approximation. Since photon paths through the atmosphere are affected by aerosols, it is essential to take the effect of aerosols on the differential slant columns into account.

Recently developed algorithms to estimate aerosol extinction profiles from MAX-DOAS observations, often depend on MAX-DOAS measurements of O_4 absorption (see e.g. Wagner et al., 2004; Sinreich et al., 2005; Friess et al., 2006; Irie et al., 2008a; Clemer et al., 2010). Absorption measurements of the collision complex of oxygen molecules, O_4, can be related via inverse modeling to the aerosol extinction profile, since O_4 absorption depends on the photon path length through the atmosphere on which aerosols have significant impact. The profile shape of O_4 is well-known, it has the shape of the squared pressure profile.

1.3 This paper

In this study, we propose a simple algorithm for a first order aerosol correction on the differential air mass factors as an alternative to the full combined retrieval of NO_2 and aerosol extinction profiles based on both O_4 and NO_2 differential slant column observations. In our algorithm, aerosol characterization, in terms of aerosol optical thickness (AOT), is based on relative intensity measurements. Relative intensity observations are defined as the ratio of the sky radiance at elevation α and the sky radiance in the zenith, and they have the advantage of a strong dependence on boundary layer AOT and almost no dependence on boundary layer height (Sect. 3.2). This characteristic of relative intensity observations distinguishes it from O_4 differential slant column measurements.

The structure of this paper is as follows: first a short description of the instrument is given, together with a characterization of the field-of-view and slit function (Sect. 2). Also the set-up of the instrument is described, the correction of measured spectra and the settings of the DOAS fit. Radiative transfer modeling of relative intensities and differential air mass factors is described in Sect. 3. A sensitivity study is performed, and error sources are discussed. Results of application of the algorithm to selected days are given in the Sect. 4. Furthermore the applicability of the geometric approximation is discussed, based on both model simulations and observations. Finally a verification of the aerosol optical thickness retrieval with AERONET data is shown, and a comparison with tropospheric NO_2 from the Ozone Monitoring Instrument (OMI).

2 Measurements

2.1 Mini MAX-DOAS instrument

The observations in this study were made with a so-called Mini MAX-DOAS instrument (e.g. Hönninger et al., 2004; Sinreich et al., 2005) produced by Hoffmann GmbH, Germany. This relatively small MAX-DOAS instrument consists essentially of a lens, optical fiber and UV/VIS spectrometer, all contained in one metal box that is mounted on a pointing mechanism (stepper motor). The instrument is designed to operate in the open air for long periods in an automated fashion. Stabilizing the temperature by cooling is made possible by a Peltier element, which cools up to 25 °C below ambient. Incoming light is focused by a lens ($f = 40$ mm) on the entrance of an optical fiber which is connected to the Ocean Optics "USB2000" crossed Czerny-Turner type spectrometer with a Sony "ILX511" CCD detector (2048 pixels). The wavelength range of the instrument is 290 to 433 nm.

Measurements with a monochromatic light source (Mercury lamp) were performed (see Fig. 2). These measurements indicated that the line shape (slit function) is asymmetric, and has a FWHM of 0.6 nm at around 408 nm. The line shape shows little

temperature dependence at this wavelength, which is not far from the spectral fitting window for NO_2 (Sect. 2.3.2).

Furthermore, the field-of-view (FOV) of the instrument was characterized (see Figs. 3 and 4). Measurements with a distant light source (−2.0 mm at 5 m) indicated that the FWHM of the FOV was around 0.45°. The pointing offset was determined from the same experiment. This pointing offset is defined as the angle between the top plane of the instrument and the horizontal plane, when the instrument is rotated such that it has maximum signal from a distant light source that is at the same height as the lens of the instrument. The pointing offset was measured each time after the instrument box was opened for maintenance and showed substantial variations (e.g. one occasion with a change from −2.0° to +0.4°) due to small displacements of the fiber entrance. The experiment was repeated including a black tube in front of the lens (not drawn), which is used normally to block stray light. Adding the tube did not change the results. The pointing offset was taken into account each time the instrument was started. The pointing of the instrument was checked on a weekly basis.

2.2 Operations

Observations were performed from the roof of the KNMI building in De Bilt, The Netherlands (52.101° N, 5.178° E), from 14 November 2007 until 29 April 2008 and from 11 September 2008 until 21 April 2009 with some days missing due to technical circumstances, resulting in 362 days of observations in total. The azimuth position of the instrument was fixed towards the North-East (at 46° azimuth relative to North). This direction was chosen for practical purposes (constraints at small elevations by trees and buildings surrounding the measurement site), and to look away from the sun for most of the day throughout the year, which is advantageous with respect to the sensitivity of the retrievals to estimated fixed parameters. Spectra were recorded at 0°, 2°, 4°, 8°, 16°, 30° and 90° elevation angles. Automated operation of the instrument was done with the DOASIS software developed by IUP Heidelberg in cooperation with Hoffmann GmbH. The integration time for each elevation was set to 30 s divided into

multiple shorter scans to prevent the detector from saturation.

2.3 DOAS analysis of spectra

2.3.1 Correction of spectra

Spectra were corrected for a CCD read-out offset. This read-out offset (or electronic offset, EO) is temperature-dependent and proportional to the number of sub-spectra that are read-out, added and stored as one spectrum. Since the instrument does not have a shutter, it was not possible to do EO and dark current measurements as a part of regular operations.

EO measurements were performed at different temperatures by reading out many spectra with minimum integration time under complete dark conditions (e.g. 1000 read-outs at 3 ms, which is the minimal read-out time of the spectrometer). These measurements demonstrated that the EO was almost constant over the whole detector range except for the first ten pixels. Since the first hundred pixels of the detector are in the far UV (below 297 nm) they are virtually blind even under atmospheric measuring conditions. A more detailed analysis showed that pixels 60–80 had an EO level that was within one percent of the offset level in the fitting window used in this study. For this reason the EO correction of each spectrum was based on an average of these pixels. An advantage of this approach is that this EO correction is less sensitive to (unknown) instabilities in the actual temperature of the instrument than if the EO correction would be based on the registered operation temperature, and an EO-temperature calibration done at another time.

It was decided not to apply a dark current (DC) correction. The DC correction depends on temperature, integration time (of each individual sub-scan) and typically shows a strong pixel to pixel variation. It requires a thermally very stable instrument to be able to correct measured spectra based on laboratory measured DC. The instrument was not expected to be thermally stable to such a high degree for the whole period of operation. The effect of applying an inappropriate dark current correction is

Title Page

Abstract | Introduction

Conclusions | References

Tables | Figures

◄ | ►

◄ | ►

Back | Close

Full Screen / Esc

comparable to applying no correction. Not applying the dark current correction in the DOAS NO$_2$ fit will in general lead to somewhat larger fit residuals but not to systematic biases. Tests on temperature-controlled measurements, under representative measurement conditions, have shown that differences between including and not including

5 DC-correction was less than 0.1% in the fitted NO$_2$ differential slant column. For other trace gases with smaller tropospheric column amounts, the effect of not correcting for dark current will be larger.

2.3.2 DOAS fitting

DOAS-fitting was performed with the "Qdoas" software developed at the Belgian Insti-

10 tute for Space and Aeronomy (IASB/BIRA) (Fayt and Van Roozendael, 2001). For each spectrum at elevation α, the nearest (in time) zenith spectrum was selected as a reference, in order to minimize the effect of unknown instrument instabilities on the DOAS fit. Since spectra were measured within 30 s to 2 min from the zenith measurement, the change in stratospheric path length was expected to be of little influence, except

15 around sunrise and sunset. The cross-sections of NO$_2$ (298 K, Vandaele et al., 1997) O$_3$ (243 K, Bogumil et al., 2003) were included in the DOAS fitting routine as well as the Ring cross-section based on a solar spectrum from Kurucz et al. (1984). Cross-sections were convoluted with the measured instrumental slit function (line shape) of the instrument. The fitting interval was 415 to 431 nm. This interval was chosen be-

20 cause NO$_2$ has relatively little interference with other absorbers in this window and because of the relatively pronounced structures in the NO$_2$ differential cross-section. It was not possible to exploit the even more pronounced structures of NO$_2$ between 430 and 450 nm, since those are just outside the detector range of the instrument. Wavelength calibration of the spectra was done in Qdoas by applying a non-linear least

25 squares fit of the spectrum to a high resolution solar spectrum (Kurucz et al., 1984) that was convoluted with the instrumental slit function.

2.4   Relative intensity observations

The observation of relative intensity of skylight is another method to derive information on atmospheric constituents from the MAX-DOAS instrument. Intensity of skylight, I, is measured here as the MAX-DOAS detector signal averaged over a certain spectral interval in one viewing direction. Only relative values of intensity can be compared to their simulated counterparts, since the instrument is not radiometrically calibrated. In this work relative intensity, I_α^{rel}, refers to the ratio of the intensity in direction α to the intensity in the zenith direction:

$$I_\alpha^{rel} = \frac{I_\alpha}{I_{90}}.$$

(4)

The wavelength interval used for I_α^{rel} was 426–429 nm, which is within the NO$_2$ DOAS fitting window, and contains the wavelength chosen for the differential air mass factor calculation (Sect. 3.1.3). In the absence of clouds, relative intensities in the visible are mainly influenced by Rayleigh scattering and aerosol scattering and absorption. Since Rayleigh scattering is accurately known, relative intensity observations contain information on aerosols, as will be shown in Sect. 3.2.

3   Retrieval algorithm

A two step approach is used to derive tropospheric vertical columns of NO$_2$ from MAX-DOAS differential slant column observations, see Fig. 5. The first step is to estimate aerosol optical thickness from relative intensity observations. This is done by interpolation of the observed relative intensity for a particular elevation and solar position (zenith and azimuth) on look-up table values of simulated relative intensity as a function of boundary layer AOT. Here it is assumed that both aerosols and tropospheric NO$_2$ are homogeneously distributed in the boundary layer. The second step is to use this

Full Screen / Esc

estimated AOT in another look-up table containing the NO$_2$ differential air mass factors for each elevation and solar position as a function of AOT.

By this method, the AOT and the tropospheric vertical column of NO$_2$ (N_α^{Tr}) are derived for each elevation independent of observations in the other elevations. A final NO$_2$ tropospheric vertical column (N^{Tr}) is found by averaging over the elevations 4°, 8° and 16°:

$$N^{Tr} = \frac{N_{4°}^{Tr} + N_{8°}^{Tr} + N_{16°}^{Tr}}{3}. \tag{5}$$

Smaller elevations were not used because the effect of the curvature of the earth is not captured by the radiative transfer model (see also Sect. 3.1.1). Larger elevations were not used because the signal-to-noise ratio of the measured differential slant column densities for this elevation was too low, namely often well below 5. This was due to the relative short integration time of 30 s, and the relative low sensitivity of the larger elevations.

As an estimate of the uncertainty on the retrieved average NO$_2$ tropospheric column we use the difference between the maximum and minimum NO$_2$ tropospheric column that is retrieved for 4°, 8° and 16° elevation (see Sect. 3.3).

3.1 Radiative transfer modeling

A multiple scattering radiative transfer model was used in this study for two purposes. Firstly to derive the look-up tables that relate relative intensity and differential air mass factors to boundary layer AOT. Those look-up tables are used in the retrieval algorithm. Secondly, to study the sensitivity of relative intensities and differential air mass factors to several parameters that cannot be retrieved and for which fixed (climatological) values are assumed.

The radiative transfer model used in this study is DAK (Doubling-Adding KNMI). The DAK model is based on the doubling-adding algorithm for multiple scattering of sunlight in a vertically inhomogeneous atmosphere with polarization included (De Haan

et al., 1987; Stammes et al., 1989). In the doubling-adding method, one starts with an optically thin layer for which the analytical solution for single and double scattering suffices to describe the radiation field. Next, subsequent doubling of this optically thin layer to an optically thick homogeneous layer, and adding different homogeneous lay-
ers together leads to a multi-layered atmosphere in which the reflected, transmitted, and internal radiation fields are calculated. In each layer, the extinction optical thickness, single scattering albedo and phase matrix (or phase function for unpolarized light) have to be prescribed. These atmospheric input parameters are calculated from temperature, pressure, trace gas mixing ratio, and aerosol profiles (Stammes, 2001).
The inclusion of polarization in computing the radiation fields is especially important in the UV and blue parts of the solar spectrum, where atmospheric Rayleigh scattering is dominating.

3.1.1 Comparison with other radiative transfer models

The DAK model was compared to the results of the model intercomparison of Wagner
et al. (2007), where a comparison of nine radiative transfer models was reported with special focus on box-air mass factors for MAX-DOAS viewing geometries. In general a good agreement was found between DAK and the models included in the comparison. A deviation from the spherical models was found only for box air mass factors in the Rayleigh atmosphere (no aerosols) at 577 nm and 2 degrees elevation (Fig. 8 from
Wagner et al., 2007). This deviation at 577 nm was consistent with the other plane parallel models. The same comparison at 360 nm showed no difference between spherical and plane-parallel models.

Based on this comparison it was concluded that the DAK simulations could be applied to the MAX-DOAS observations at around 425 nm for elevations of 4 degrees and
above.

3.1.2 Parameter settings

In the algorithm and radiative transfer model, several parameters were assumed fixed. These are also the standard settings in the sensitivity study of Sect. 3.2. These parameters are:

(a) Block functions to describe the aerosol extinction profile and NO_2 profile in the planetary boundary layer (layer height: 1.0 km); (b) US-standard mid-latitude summer profiles for temperature and pressure at all heights and for NO_2 above 5 km; (c) NO_2 tropospheric vertical column is 2×10^{16} molecules/cm^2; (d) Aerosol characterization: single scattering albedo is 0.92, asymmetry parameter is 0.70, Henyey-Greenstein phase function; (e) Surface albedo is 0.06; (f) Effect of linear polarization is included. The choice for this single scattering albedo and asymmetry parameter was based on AERONET observations from the Cabauw site (22 km from instrument location), for fourteen blue sky days in the years 2007–2009 throughout the various seasons.

3.1.3 Calculation of differential AMF

The differential air mass factor was calculated for one effective wavelength (428.22 nm), and this differential AMF was assumed to be representative for the whole fitting window 415–431 nm. Assumptions with respect to the model atmosphere for which differential AMFs and relative intensities were calculated, are described in the previous section.

The differential air mass factor was calculated in a way that is somewhat different from the conventional method where a differential AMF (ΔM_α) for an elevation is found by subtracting from its AMF (M_α) the zenith-AMF ($M_{90°}$). In the case of this conventional method, the AMF itself is derived from two radiative transfer simulations: one for an atmosphere excluding NO_2, and another one for an atmosphere including NO_2, assuming a specific vertical distribution of NO_2.

In our study an approach is followed which is numerically equivalent to the conventional method within one percent. It was chosen because it closely resembles the MAX-DOAS method, where differential slant columns are derived directly from spectra

Title Page

Abstract | Introduction

Conclusions | References

Tables | Figures

|◄ | ►|

◄ | ►

Back | Close

Full Screen / Esc

Printer-friendly Version

Interactive Discussion

in two viewing directions: one spectrum measured at elevation α and one zenith reference spectrum. Radiative transfer calculations were performed for just one atmosphere, including an assumed NO_2 vertical profile. Three wavelengths (426.48, 428.22 and 429.86 nm) were used to be able to subtract a background absorption spectrum, which also includes the low-pass filtered (or broad band) absorption by NO_2. In this way, a simulated differential slant column can be derived from the ratio of the differential absorption slant optical thickness to the differential cross-section of NO_2. The three wavelengths were chosen such that they were close together, at local maximum and minima of the NO_2 cross-sections, and within the DOAS spectral fitting window in which the measurements are analyzed (see Fig. 6).

The derivation of the differential AMF is as follows. We assume that the light paths in the atmosphere are not changed when adding a relatively weak absorber like NO_2. The sky radiance for elevation α and wavelength λ with NO_2 in the atmosphere ($I_\alpha(\lambda)$) is equal to the sky radiance without NO_2 ($I_\alpha^0(\lambda)$) times an attenuation term depending on the NO_2 slant column for this elevation (N_α^S), and the NO_2 absorption cross-section ($\sigma(\lambda)$) at this wavelength:

$$I_\alpha(\lambda) = I_\alpha^0(\lambda)\, e^{-N_\alpha^S \sigma(\lambda)}, \tag{6}$$

also known as the law of Bouguer-Lambert-Beer. Taking the natural logarithm of the ratio of the radiances at elevation α and the zenith ($\alpha=90°$), and writing:

$$R_\alpha^{(0)}(\lambda) = \ln\left[\frac{I_\alpha^{(0)}(\lambda)}{I_{90°}^{(0)}(\lambda)}\right], \tag{7}$$

and

$$\Delta N_\alpha^S = N_\alpha^S - N_{90°}^S, \tag{8}$$

leads to:

$$R_\alpha(\lambda) = R_\alpha^0(\lambda) - \Delta N_\alpha^S \sigma(\lambda). \tag{9}$$

Title Page

Abstract | Introduction

Conclusions | References

Tables | Figures

|◄ | ►|

◄ | ►

Back | Close

Full Screen / Esc

Printer-friendly Version

Interactive Discussion

This equation may be written for the three wavelengths $\lambda_1 = 426.48$ nm, $\lambda_2 = 428.22$ nm and $\lambda_3 = 429.86$ nm. $R_\alpha^{(0)}$ and σ can be interpolated to λ_2, using the values at λ_1 and λ_3, which leads to a second equation defined at λ_2. The two equations at λ_2 are:

$$R_\alpha(\lambda_2) = R_\alpha^0(\lambda_2) - \Delta N_\alpha^S \sigma(\lambda_2), \tag{10}$$

and

$$R_\alpha^*(\lambda_2) = R_\alpha^{0*}(\lambda_2) - \Delta N_\alpha^S \sigma^*(\lambda_2), \tag{11}$$

where the * refers to the interpolated values at λ_2. Now we assume that in this short interval, R^0 can be approximated by a linear function, since it is not affected – in the model atmosphere – by absorbers with a fine-scale structure. Consequently:

$$R_\alpha^{0*}(\lambda_2) = R_\alpha^0(\lambda_2). \tag{12}$$

If we define

$$\Delta R_\alpha(\lambda_2) = R_\alpha(\lambda_2) - R_\alpha^*(\lambda_2), \tag{13}$$

and

$$\Delta\sigma(\lambda_2) = \sigma^*(\lambda_2) - \sigma(\lambda_2), \tag{14}$$

(see Fig. 6), take the difference of Eqs. (10) and (11), and make use of Eq. (2), we find the following expression for the differential air mass factor (ΔM_α) at elevation α:

$$\Delta M_\alpha(\lambda_2) = \frac{\Delta R_\alpha(\lambda_2)}{N^{\mathrm{Tr}}\Delta\sigma(\lambda_2)}. \tag{15}$$

3.2 Sensitivity study

A sensitivity study was performed to quantify the effect of variations in several parameters on the differential air mass factors, relative intensities and the combined steps in

Title Page

Abstract | Introduction

Conclusions | References

Tables | Figures

|◄ | ►|

◄ | ►

Back | Close

Full Screen / Esc

Printer-friendly Version

Interactive Discussion

the algorithm that lead to the retrieved tropospheric NO$_2$ column. These parameters were: boundary layer height, tropospheric NO$_2$ vertical column, aerosol optical thickness, asymmetry parameter, single scattering albedo, surface albedo and polarization. In each DAK model run only one parameter was changed with respect to the standard settings described in Sect. 3.1.2. The range of the variation of each parameter is given by columns case 1 and case 2 in Table 1.

The first column of each elevation (4°, 8°, 16°) in this table gives the sensitivity of the relative intensity to a parameter change from case 1 to case 2 (where all other parameters do not change), and each second column gives the sensitivity of the differential air mass factor. The third column of each elevation shows the sensitivity of the retrieved tropospheric NO$_2$ column for that elevation.

Table 1 shows that both the relative intensity and the differential AMF are most sensitive to the amount of boundary layer aerosols, as seen by the effect of a change in the aerosol optical thickness. The retrieval of tropospheric NO$_2$ columns however, is insensitive to a change in AOT, since the algorithm is designed to correct for this change. Figure 7 shows the effect of the AOT on relative intensity and differential AMF in more detail.

The sensitivity to a simultaneous change of both the NO$_2$ and aerosol vertical block profiles is given in the second line of Table 1. This shows that relative intensity observations – and thus the AOT retrieval – are quite insensitive to a change in boundary layer height, when compared with the sensitivity to a change in AOT (first line). However, the combined effect of relative intensity and differential AMF leads to a relatively large change in the tropospheric NO$_2$ column, especially for 4° elevation. If only the NO$_2$ vertical block profile is changed with respect to the reference situation (third line), then there is a larger change of the differential AMF and the retrieved tropospheric NO$_2$ column. This underlines that knowledge of the NO$_2$ profile shape is crucial to have an accurate tropospheric NO$_2$ column retrieval.

Measured differential slant columns are influenced not only by the vertical profile shape of NO$_2$, but also by the vertical sensitivity to NO$_2$. A useful quantity to describe

the sensitivity to NO$_2$ at various altitudes is the height-dependent air mass factor, a quantity that is also referred to as (differential) box-AMF (see e.g. Hönninger et al., 2004; Wagner et al., 2007). The height-dependent differential AMF ($\Delta m_\alpha(z)$) at height z for elevation α, was calculated by perturbing the background NO$_2$ profile at height z:

$$\Delta m_\alpha(z) = \frac{[\Delta M_\alpha]^{z+} - [\Delta M_\alpha]^{\text{ref}}}{[N^V]^{z+} - [N^V]^{\text{ref}}}, \tag{16}$$

where the superscript "ref" refers to a simulation for a background NO$_2$ profile, and the superscript $z+$ refers to a simulation where NO$_2$ is added to the background profile at height z.

Figure 8 shows the differential box-AMF for different elevations and for two values of the AOT (see also Wittrock et al., 2004, and Pikelnaya et al., 2007, for similar results obtained with different radiative transfer models). The low elevations have a sensitivity to NO$_2$ that decreases rapidly with height, whereas the vertical sensitivity of the higher elevations is more constant. Increasing the amount of aerosols in the boundary layer leads, for the low elevations, to a pronounced decrease in sensitivity to NO$_2$ with increasing altitude.

Figure 9 shows the dependence of relative intensity on boundary layer height and aerosol optical thickness, for two elevations (4° and 30°). The relatively weak sensitivity of relative intensity to a change in boundary layer height, is the reason that relative intensity observations are more suitable for boundary layer aerosol optical thickness estimations than measurements of O$_4$. A relative intensity observation of only a single elevation is needed to estimate the aerosol optical thickness. O$_4$ observations on the other hand, contain more information on the aerosol profile, which is the reason why they are used in MAX-DOAS aerosol extinction profile retrievals (Friess et al., 2006; Irie et al., 2008a; Clemer et al., 2010).

From the fourth line in Table 1 it appears that there is an unwanted dependence of the algorithm to the tropospheric NO$_2$ column itself. This can be solved by making the algorithm iterative, with the tropospheric NO$_2$ column as an additional dimension of the

look-up table, but this step was not applied in this study.

Finally, Table 1 shows that the asymmetry parameter, single scattering albedo, surface albedo and polarization have a relatively small effect on the retrieved tropospheric NO$_2$ column.

Table 1 was calculated for a relative azimuth of 180° and a solar zenith angle of 60°. Additional studies showed that the values in the table are representative for other solar positions except when the instrument is viewing in a direction close to the sun (either in viewing direction α, or in the zenith direction) where simulated quantities depend more critically on the aerosol model parameters. Since the Mini MAX-DOAS instrument was pointed towards the North-East, the sun was at relatively large angular distance for most of the time.

3.3 Error sources

There are many possible sources of error in the retrieval of NO$_2$ tropospheric columns from MAX-DOAS observations. Two types of error may be distinguished: observational errors and modeling errors. The term observational error is used here for all factors leading to an incorrect value for the differential slant column and/or relative intensity.

Systematic error contributions to the observational error are: (1) errors caused by incorrect knowledge of the actual field-of-view, which may be caused by incorrect aiming of the instrument (e.g. when it is unattended after periods of heavy winds) or by imprecise knowledge of the offset in the field-of-view as described in Sect. 2.1, (2) incorrect electronic offset correction of raw spectra, (3) errors in the differential cross-sections of NO$_2$ (e.g. temperature dependency). The DOAS spectral-fitting error represents a mixture of systematic and random errors: incorrect wavelength calibration of spectra, inaccurate knowledge of instrument slit function, incorrect dark current correction, unknown absorbers, and low signal-to-noise.

The DOAS fitting was performed with a cross section at a fixed temperature (see Sect. 2.3.2). This introduces an error in the differential slant column of NO$_2$ that is proportional to the temperature difference between the fixed temperature of the cross

section used in the fit and the effective temperature of the tropospheric NO_2. Although the NO_2 cross section σ_{NO_2} itself is not strongly temperature dependent, the differential cross section $\Delta\sigma_{NO_2}$ shows a much stronger temperature dependence: a change in temperature of 20 degrees corresponds to a change in σ_{NO_2} of 1.6% and to a change in $\Delta\sigma_{NO_2}$ of 7.2%. An estimate of the effective NO_2 temperature is needed to correct for this effect (see Sect. 4.4).

The modeling errors that affect the differential AMF are introduced in two ways: first by not including parameters in the radiative transfer modeling that do have an effect on the observations, and second by choosing inappropriate values for parameters that are included in the model. Some examples of parameters that were not included in the model are: humidity, clouds, horizontal gradients in all parameters of which a vertical profile is prescribed, and vertical profile shapes other than those described in Sect. 3.1.2.

The effect of inaccurate estimation of the included model parameters was studied in Sect. 3.2. The algorithm described in this study is most sensitive to the boundary layer height, especially to the vertical profile shape of NO_2. This is a consequence of the decrease in sensitivity to NO_2 with increasing height, especially for low elevations (see e.g. Wittrock et al., 2004, their Fig. 4).

In this study, we estimate the uncertainty ε on the retrieved average NO_2 tropospheric column (Eq. 5) as the difference between the maximum and minimum NO_2 tropospheric column that is retrieved for 4°, 8° and 16° elevation:

$$\varepsilon = \max\left(N^{Tr}_{[4°,8°,16°]}\right) - \min\left(N^{Tr}_{[4°,8°,16°]}\right), \tag{17}$$

where the three tropospheric columns are interpolated to the same point in time. Since the tropospheric columns are derived for each elevation independent of the others, this difference, or spread, gives an important indication of the internal consistency of the retrieval. A small spread indicates a consistent retrieval. The spread increases for measurement conditions that differ from the model atmosphere in the look-up table calculations. For instance, an error in the assumed boundary layer height would

lead to different systematic errors in the retrieved tropospheric NO$_2$ columns for each elevation angle (see Table 1). This would result in a systematic error in the derived average tropospheric NO$_2$ column and an increase in the spread. The definition of the measurement uncertainty includes effects such as: presence of clouds, pointing elevation offsets, horizontal gradients, vertical profile shape of aerosols and NO$_2$, and uncertainty due to a low signal-to-noise.

Typical values of ε are on average much lower for clear sky than for cloudy conditions (see Sect. 4.1). If data is selected for clear sky conditions, using the criterion that the relative intensity of 4°, 8° and 16° is > 1, then the median of the measurement uncertainty ε is 2.7×10^{15} molecules/cm^2 or 17% relative to a mean tropospheric NO$_2$ column of 15.6×10^{15} molecules/cm^2.

4 Results

In this section various results of our new two-step algorithm will be shown. Firstly, several steps in the tropospheric NO$_2$ retrieval algorithm will be illustrated for three selected days, and AOT and tropospheric NO$_2$ retrievals will be shown for four more days. Secondly, the algorithm is compared to the geometrical approximation, which is the default approach to derive tropospheric columns from MAX-DOAS observations. Finally a comparison with AOT from an AERONET instrument and a comparison with OMI tropospheric NO$_2$ is shown.

4.1 AOT and tropospheric NO$_2$ for selected days

Figure 10 shows the differential slant columns of NO$_2$, relative intensity, aerosol optical thickness and tropospheric NO$_2$ columns for three days, to illustrate the different steps in the retrieval. The first day (12 October 2008) is selected to illustrate the effect of clouds on the retrieval. Until around 13:00 UTC, clouds where present above the measurement location. This can be seen most clearly from the relative intensity

observations. Under a homogeneous cloud cover, the intensity of scattered light is higher in the zenith direction than in other directions, and is decreasing with decreasing elevation. This results in relative intensities < 1. After the clouds disappear (around 13:00 UTC) the situation is opposite. Under clear sky conditions the intensity of the scattered sunlight above the horizon is generally higher than the intensity in the zenith; the maximum intensity occurs usually somewhere between $\alpha = 8°$ and $\alpha = 25°$, depending on e.g. solar position and AOT (see Fig. 7). For this reason relative intensity > 1 is a good first indication for clear sky conditions, although this is not true in general: for small solar zenith angles the zenith sky may be brighter than the horizon.

It is to be expected that relative intensity cannot be used to retrieve AOT under cloudy circumstances since the cloud has a much stronger effect on the relative intensity than the aerosols. As a consequence, AOT values larger than the maximum AOT of the lookup table (0.8) are retrieved before 13:00 UTC on 12 October 2008. At later times the three elevations (4°, 8°, 16°) give similar AOT values. The effect of too large AOTs can also be seen in the NO$_2$ tropospheric column retrieval for this day. However, a sudden change between 12:00 and 13:00 UTC cannot be seen in the differential slant columns. This illustrates that differential slant column measurements are mostly sensitive to the lowest kilometers of the atmosphere (whether or not below a cloud). The other two days in Fig. 10 (26 December 2008 and 27 January 2009) are included as an example of both a relatively clean and a relatively polluted day. The clean day, December 26, was a public holiday with temperatures below 0 °C. It shows stable conditions in both the tropospheric NO$_2$ column and AOT.

Four more examples of retrievals for cloud free days are shown in Fig. 11. The spread in the tropospheric columns of NO$_2$ between the three different elevations is relatively small, about 10%. Possible causes of the spread are discussed in Sect. 3.3.

4.2 Comparison with geometrical air mass factor approximation

The geometrical approximation (GA) of the differential air mass factor for MAX-DOAS observations provides a simple way to determine a first order estimate of the

tropospheric column of NO$_2$, or other trace gases that are located primarily in the boundary layer. It is applied to MAX-DOAS observations in e.g. Brinksma et al. (2008) and Hains et al. (2010) in a comparison with other methods to measure tropospheric NO$_2$, such as lidar and satellite.

Using the geometric approximation is simple: it does not require an inversion based on radiative transfer modeling. The question remains how accurate this approximation is. This issue has been discussed by e.g. Hönninger et al. (2004), Wittrock et al. (2004), and Pinardi et al. (2008), based primarily on radiative transfer modeling results.

Here we follow a different approach, partly based on observations. Simulations with DAK show that, depending on the boundary layer aerosol load, large differences may occur between the geometrical and modeled differential air mass factors at low elevations: $\alpha \leq 16°$, (see Fig. 7, right plot). Therefore the GA should not be used for these elevations. For higher elevations, the difference becomes much smaller. It seems from Fig. 7 that the radiative transfer model and the GA have almost the same differential air mass factor for 30° elevation. However, it can be seen from Fig. 12 that even for this high elevation, the difference between the GA and the model may become as large as 25%, depending on the relative position of the sun. At smaller relative azimuths this relative difference is even higher.

The effect of the difference between the geometrical approximation and radiative-transfer based and aerosol corrected differential air mass factors can also be observed in the measurements. Figure 13 shows that the tropospheric column of NO$_2$ derived from the GA for $\alpha=30°$, is not in agreement with the tropospheric column derived with the algorithm using the mean of $\alpha=4°$, 8° and 16°. The algorithm finds a NO$_2$ tropospheric column that is significantly different from the geometrical approximation, with differences up to 20%.

To find out whether this difference could be due to the difference in differential slant columns, the tropospheric NO$_2$ column is calculated from the differential slant column at 30° (that were only used before in combination with the GA) with the differential air mass factor calculated according to the two-step algorithm. Thus for this specific study,

T. Vlemmix et al.

the algorithm is applied to 30° elevation alone. Figure 13 shows that this method to calculate the tropospheric NO$_2$ vertical column is better in agreement with the tropospheric columns derived with the standard algorithm than the GA.

It can be concluded that the geometrical approximation is not sufficiently accurate for tropospheric NO$_2$ retrieval. However, it can be used for a quick indicative conversion from the differential slant column at 30° to a tropospheric column. A disadvantage in using this (relatively high) elevation is the reduced sensitivity to the lower troposphere.

4.3 Verification of AOT with AERONET data

As a verification of the AOT retrieved by the new two-step algorithm, a comparison is shown in Fig. 14 between the AOT data from the MAX-DOAS observations of relative intensity at De Bilt and the AOT data from the Aerosol Robotic Network (AERONET, see Dubovik and King, 2000) instrument at Cabauw (22 km from De Bilt). For all days in the operational period (see Sect. 2.2) level 1.5 AERONET AOT data at 440 nm was selected (if available) and compared with MAX-DOAS AOT data if the uncertainty in this value – i.e. the spread between AOTs derived from $\alpha=4°$, 8° and 16° – was below 0.1. This selection resulted in 1251 data points with a correlation of 0.85. The mean difference between the AERONET and MAX-DOAS AOT was −0.01 with a standard deviation of 0.08. Next, a linear regression was done that minimizes the sum of the squared orthogonal distances. From this regression a slope of 1.01 was found and an offset of −0.01. Considering the difference in observation method (direct sunlight versus scattered sunlight), and the distance between the two sites, this agreement is satisfying.

4.4 Comparison with satellite observations

As a first application of the time series of tropospheric NO$_2$ columns derived from the Mini MAX-DOAS measurements in De Bilt, an inter-comparison was made with tropospheric NO$_2$ data (DOMINO-product, see Boersma et al., 2007) from the Ozone

Monitoring Instrument (OMI, see Levelt et al., 2006). The DOMINO data selection was based on the following criteria: the satellite cloud fraction should be below 0.2 and the NO_2 slant column should be below 2×10^{17} molec/cm^2. Pixels affected by the OMI row-anomaly were removed. A coincident ground and satellite observation was defined

5 as a measurement where the ground site was within the satellite pixel (which has an approximate rectangular shape, ranging from 13×24 km^2 at nadir to 26×135 km^2 at the edge of the swath (Dobber et al., private communication)). The ground-based tropospheric column was averaged over 15 min around the time of satellite overpass.

A correction was applied to account for the fixed temperature dependence of the

10 NO_2 cross section (see Sect. 2.3.2). Two steps were taken to estimate the effective NO_2 temperature at the time of observation.

First the difference was determined between the surface temperature and the effective NO_2 temperature $T_{NO_2}^{eff}$:

$$T_{NO_2}^{eff} = \frac{\int T(z)m(z)n(z)dz}{\int m(z)n(z)dz}, \qquad (18)$$

15 where $m(z)$ is the the height-dependent differential air mass factor for an AOT of 0.2 (see Fig. 8), $n(z)$ is a block profile for NO_2 from 0–1 km, and $T(z)$ is a standard temperature profile. A difference of about $-2.5\,°C$ was found between the surface temperature and the effective NO_2 temperature for all three elevations 4°, 8° and 16°.

Then surface temperature data were taken from KNMI temperature observations in

20 De Bilt, and from this $2.5\,°C$ was subtracted to determine the effective NO_2 temperature. The ratio of $\Delta\sigma$ (see Fig. 6) at the temperature of the NO_2 cross section in the DOAS-fit and $\Delta\sigma$ at the effective NO_2 temperature was applied as a temperature correction factor to the MAX-DOAS tropospheric NO_2 columns.

Figure 15 shows a scatter plot of the comparison. Three different selections of the

25 MAX-DOAS data were made, based on different constraints on the (relative) spread of the ground-based tropospheric column of NO_2 (see Table 2). From 362 days of ground-based observations (see Sect. 2.2) only 123 data points remain after applying

the selection criteria on the satellite data (including coincidence with the ground-based observation). Only 17 ground-based observations pass the 10% threshold, as described in Table 2.

The table shows that the correlation between the ground-based and satellite data improves with a more strict selection of the ground-based observations. However, when the estimated uncertainty (spread) of the ground-based observations is less than 10%, the standard deviation of the differences between the two data sets is about 25% (3.8×10^{15} molec/cm^2 for a mean value of about 15×10^{15} molec/cm^2).

To test if the spread between the OMI and the MAX-DOAS tropospheric NO$_2$ columns is dominated by the estimated retrieval errors from both data sets, a χ^2 test was applied:

$$\chi_v^2 = \frac{1}{N} \sum_{i=1}^{N} \frac{(x_i - y_i)^2}{\varepsilon_{x_i}^2 + \varepsilon_{y_i}^2}, \tag{19}$$

where N is the number of data points (x_i, y_i), x_i is an OMI tropospheric NO$_2$ column measurement, with retrieval error ε_{x_i}, and y_i is a MAX-DOAS tropospheric NO$_2$ column measurement with retrieval error ε_{y_i} estimated from the spread as described in Eq. (17). For the three selections of the data, as described in Table 2, χ_v^2 is between 2.5 and 3. Assuming an average difference of zero between the data sets and normal error distributions, the probability of exceeding these values for χ_v^2 is less than 0.1%. Hence, the spread is larger than can be expected from the estimated retrieval errors alone.

A possible explanation for the part of the spread that is not explained by the retrieval errors, is the difference in observation techniques. First, the spatial representativity of the two types of observation is quite different. The horizontal footprint of an OMI pixel is different from the horizontal domain of the MAX-DOAS observation. Whereas OMI samples a domain of $> 300\,\text{km}^2$, the MAX-DOAS has a horizontal range – in one direction – of roughly 10 km for the lowest elevation of 4°. Also the vertical range that

Title Page

Abstract | Introduction

Conclusions | References

Tables | Figures

◀ | ▶

◀ | ▶

Back | Close

Full Screen / Esc

Printer-friendly Version

Interactive Discussion

contributes to the tropospheric NO_2 signal is different for the satellite and the MAX-DOAS observations. The sensitivity of MAX-DOAS to NO_2 decreases quickly with increasing height of NO_2, especially for high aerosol loads (see Fig. 8), whereas the satellite has increasing sensitivity with increasing NO_2 height (Eskes and Boersma, 2003). Consequently, the relative contribution of the free-tropospheric NO_2 to the total tropospheric NO_2 is different for the satellite than for MAX-DOAS.

Separation of the free tropospheric and boundary layer contribution to the tropospheric NO_2 column requires accurate knowledge of the NO_2 profile shape, both for the satellite and the MAX-DOAS retrieval. Lack of knowledge of the vertical distribution of NO_2 thus complicates the comparison of satellite and MAX-DOAS NO_2-data as well as the interpretation of satellite retrievals in terms of surface concentrations.

More observations and understanding of vertical profiles of NO_2 are needed to study the variety of circumstances under which differences between satellite and ground-based observations occur.

5 Conclusions

We described a new two-step algorithm to retrieve aerosol corrected tropospheric NO_2 columns from MAX-DOAS observations.

We used relative intensity observations performed with a mini MAX-DOAS instrument to estimate the aerosol optical thickness of the boundary layer. Based on this AOT-estimation, aerosol corrected differential air mass factors for NO_2 were determined to convert differential slant columns of NO_2 to tropospheric columns.

Relative intensity measurements have a strong dependence on boundary layer AOT and almost no dependence on boundary layer height although this dependence increases slightly with decreasing elevation.

Since relative intensity observations are very sensitive to clouds, the retrieval method can only be applied to cloud-free conditions. Under cloud-free conditions, the main source of error is the assumption of a fixed boundary layer height for NO_2 in the

algorithm. An uncertainty estimate in the results is derived from the spread in the tropospheric NO_2 columns that are derived independently for each elevation (4°, 8° and 16°). A low spread indicates a consistent retrieval of the tropospheric NO_2 column for the three elevations.

5 The use of the relatively low elevations makes the retrieval method more sensitive to trace gases in the boundary layer than the often used geometrical approximation that can only be applied at higher elevations (30°). The geometrical air mass factor approximation for 30° elevation gives a good first estimate of the tropospheric column. However, even for this high elevation, the differential air mass factor of the geometrical

10 approach may differ up to 25% from the differential air mass factors using radiative transfer modeling. For relative azimuths smaller than 40°, this difference may even be larger.

The relatively low-cost (Mini) MAX-DOAS instruments are capable of generating long time-series of tropospheric composition data in an automated fashion. MAX-DOAS ob-

15 servations are particularly valuable for the purpose of satellite validation of tropospheric trace gases due to the horizontal and vertical range where trace gases can be detected, which is on the order of 1 to 4 km in the vertical and 5 to 10 km in the horizontal, depending on the AOT. Accurate comparison of satellite and ground-based observations requires knowledge of the NO_2 profile shape, in order to account for differences in the

20 sensitivity to NO_2 at different heights.

The two-step retrieval scheme presented here was applied to cloud-free periods in a twelve month data set of MAX-DOAS observations in De Bilt, the Netherlands, between Autumn 2007 and Spring 2009 (summer of 2008 not included). For cloud free periods, the average tropospheric NO_2 column was 15.6×10^{15} molecules/cm^2. The median of

25 the estimated relative uncertainty was 17%.

In a comparison with AERONET (Cabauw site, 22 km from De Bilt) a mean difference in AOT (AERONET minus MAX-DOAS) of -0.01 ± 0.08 was found, and a correlation of 0.85.

Tropospheric NO_2 columns were compared with OMI satellite tropospheric NO_2. Only satellite pixels over De Bilt were selected. The spread in the tropospheric NO_2 columns retrieved (semi)-simultaneously from the different MAX-DOAS elevations was used as a selection criterion. For ground-based observations restricted to a spread below 10%, a correlation of 0.88 was found, and no significant difference. The spread between OMI and MAX-DOAS tropospheric NO_2 column measurements is larger than can be expected from the estimated retrieval errors alone. This may be due to differences in the spatial representativity of the two observation techniques.

Title Page

Abstract | Introduction

Conclusions | References

Tables | Figures

◄ | ►

◄ | ►

Back | Close

Full Screen / Esc

Printer-friendly Version

Interactive Discussion

References

Blond, N., Boersma, K. F., Eskes, H. J., van der A, R. J., Van Roozendael, M., De Smedt, I., Bergametti, G., and Vautard, R.: Intercomparison of SCIAMACHY nitrogen dioxide observations, in situ measurements and air quality modeling results over Western Europe, J. Geophys. Res., 112, D10311, doi:10.1029/2006JD007277, 2007. 2319

Boersma, K. F., Eskes, H. J., and Brinksma, E. J.: Error analysis for tropospheric NO2 retrieval from space, J. Geophys. Res., 109, D04311, doi:10.1029/2003JD003962, 2004. 2319

Boersma, K. F., Eskes, H. J., Veefkind, J. P., Brinksma, E. J., van der A, R. J., Sneep, M., van den Oord, G. H. J., Levelt, P. F., Stammes, P., Gleason, J. F., and Bucsela, E. J.: Near-real time retrieval of tropospheric NO2 from OMI, Atmos. Chem. Phys., 7, 2103–2118, doi:10.5194/acp-7-2103-2007, 2007. 2340

Boersma, K. F., Jacob, D. J., Eskes, H. J., Pinder, R. W., Wang, J., and van der A, R. J.: Intercomparison of SCIAMACHY and OMI tropospheric NO2 columns: Observing the diurnal evolution of chemistry and emissions from space, J. Geophys. Res., 113, D16S26, doi:10. 1029/2007JD008816, 2008. 2319

Bogumil, K., Orphal, J., Homann, T., Voigt, S., Spietz, P., Fleischmann, O. C., Vogel, A., Hartmann, M., Kromminga, H., Bovensmann, H., Frerick, J., and Burrows, J. P.: Measurements of Molecular Absorption Spectra with the SCIAMACHY Pre-Flight Model: Instrument Characterization and Reference Data for Atmospheric Remote-Sensing in the 230-2380 nm Region, J. Photochem. Photobiol. A., 157, 167–184, 2003. 2326

Brinksma, E. J., Pinardi, G., Volten, H., Braak, R., Richter, A., Schoenhardt, A., Van Roozendael, M., Fayt, C., Hermans, C., Dirksen, R. J., Vlemmix, T., Berkhout, A. J. C., Swart, D. P. J., Oetjes, H., Wittrock, F., Wagner, T., Ibrahim, O., de Leeuw, G., Moerman, M., Curier, R. L., Celarier, E. A., Cede, A., Knap, W. H., Veefkind, J. P., Eskes, H. J., Allaart, M., Rothe, R., Piters, A. J. M., and Levelt, P. F.: The 2005 and 2006 DANDELIONS NO2 and aerosol intercomparison campaigns, J. Geophys. Res., 113, D16S46, doi:10.1029/2007JD008988, 2008. 2319, 2322, 2339

Clémer, K., Van Roozendael, M., Fayt, C., Hendrick, F., Hermans, C., Pinardi, G., Spurr, R., Wang, P., and De Mazière, M.: Multiple wavelength retrieval of tropospheric aerosol optical properties from MAXDOAS measurements in Beijing, Atmos. Meas. Tech. Discuss., 3, 111–145, doi:10.5194/amtd-3-111-2010, 2010. 2322, 2334

De Haan, J. F., Bosma, P. B., and Hovenier, J. W.: The adding method for multiple scattering

Title Page

Abstract | Introduction

Conclusions | References

Tables | Figures

◄◄ | ►►

◄ | ►

Back | Close

Full Screen / Esc

Printer-friendly Version

Interactive Discussion

calculations of polarized light, Astron. Astrophys., 183, 371–393, 1987. 2328

Dubovik, O. and King, M. D.: A flexible inversion algorithm for retrieval of aerosol optical properties from Sun and sky radiance measurements, J. Geophys. Res., 105(D16), 673–696, doi:10.1029/2000JD900282, 2000. 2340

Eskes, H. J. and Boersma, K. F.: Averaging kernels for DOAS total-column satellite retrievals, Atmos. Chem. Phys., 3, 1285–1291, doi:10.5194/acp-3-1285-2003, 2003. 2343

Fayt, C. and Van Roozendael, M.: WinDOAS 2.1: Software User Manual, http://www.oma.be/BIRA-IASB/Molecules/BrO/WinDOAS-SUM-210b.pdf, 2001. 2326

Friess, U., Monks, P. S., Remedios, J. J., Rozanov, A., Sinreich, R., Wagner, T., and Platt, U.: MAX-DOAS O_4 measurements: A new technique to derive information on atmospheric aerosols: 2. Modeling studies, J. Geophys. Res., 111, D14203, doi:10.1029/2005JD006618, 2006. 2320, 2322, 2334

Hains, J., Boersma, K. F., Kroon, M., and Dirksen, R. J.: Testing and Improving OMI DOMINO Tropospheric NO2 Using Observations from the DANDELIONS and INTEX-B Validation Campaigns, J. Geophys. Res., 115, D05301, doi:10.1029/2009JD012399, 2010. 2319, 2322, 2339

Herman, J., Cede, A., Spinei, E., Mount, G., Tzortziou, M., and Abuhassan, N.: NO2 column amounts from ground-based Pandora and MFDOAS spectrometers using the direct-sun DOAS technique: Intercomparisons and application to OMI validation, J. Geophys. Res., 114, D13307, doi:10.1029/2009JD011848, 2009. 2320

Hönninger, G., von Friedeburg, C., and Platt, U.: Multi axis differential optical absorption spectroscopy (MAX-DOAS), Atmos. Chem. Phys., 4, 231–254, doi:10.5194/acp-4-231-2004, 2004. 2320, 2321, 2323, 2334, 2339

Irie, H., Kanaya, Y., Akimoto, H., Iwabuchi, H., Shimizu, A., and Aoki, K.: First retrieval of tropospheric aerosol profiles using MAX-DOAS and comparison with lidar and sky radiometer measurements, Atmos. Chem. Phys., 8, 341–350, doi:10.5194/acp-8-341-2008, 2008a. 2320, 2322, 2334

Irie, H., Kanaya, Y., Akimoto, H., Tanimoto, H., Wang, Z., Gleason, J. F., and Bucsela, E. J.: Validation of OMI tropospheric NO_2 column data using MAX-DOAS measurements deep inside the North China Plain in June 2006: Mount Tai Experiment 2006, Atmos. Chem. Phys., 8, 6577–6586, doi:10.5194/acp-8-6577-2008, 2008b. 2319

Kurucz, R. L., Furenlid, I., and Testerman, L.: Solar Flux Atlas from 296 to 1300 nm, Technical Report, National Solar Observatory, 1984. 2326

MAX-DOAS aerosol corrected tropospheric NO$_2$ columns

T. Vlemmix et al.

Title Page

Abstract	Introduction
Conclusions	References
Tables	Figures

|◄ | ►|

◄ | ►

Back | Close

Full Screen / Esc

Printer-friendly Version

Interactive Discussion

Leigh, R. J., Corlett, G. K., Frieß, U., and Monks, P. S.: Spatially resolved measurements of nitrogen dioxide in an urban environment using concurrent multi-axis differential optical absorption spectroscopy, Atmos. Chem. Phys., 7, 4751–4762, doi:10.5194/acp-7-4751-2007, 2007. 2320

5 Levelt, P. F., van den Oord, G. H. J., Dobber, M., Mälkki, A., Visser, H., de Vries, J., Stammes, P., Lundell, J., and Saari, H.: The Ozone Monitoring Instrument, IEEE Trans. Geo. Rem. Sens., 44, 1093–1101, 2006. 2341

Martin, R. V., Jacob, D. J., Chance, K., Kurosu, T. P., Palmer, P. I., and Evans, M. J.: Global inventory of nitrogen oxide emissions constrained by space-based observations of NO2

10 columns, J. Geophys. Res., 108, D17, doi:10.1029/2003JD003453, 2003. 2319

Melo, S. M. L., Strong, K., Bassford, M. R., Preston, K. E., McElroy, C. T., Rozanov, E. V., and Egorova, T.: Retrieval of Stratospheric NO$_2$ Vertical Profiles from Ground-Based Zenith-Sky DOAS Measurements: Results for the MANTRA 1998 Field Campaign, Atmosphere-Ocean, 43, 340–350, 2005. 2320

15 Mijling, B., van der A, R. J., Boersma, K. F., Van Roozendael, M., Desmedt, I., and Kelder, H. M.: Reductions of NO$_2$ Detected from Space During the 2008 Beijing Olympic Games, Geophys. Res. Lett., 36, L13801, doi:10.1029/2009GL038943, 2009. 2319

Pikelnaya, O., Hurlock, S. C., Trick, S., and Stutz, J.: Intercomparison of multiaxis and long-path optical absorption spectroscopy measurements in the marine boundary layer, J. Geophys.

20 Res., 112, D10S01, doi:10.1029/2006JD007727, 2007. 2320, 2334

Pinardi, G., Hendrick, F., Clemer, K., Lambert, J. C., Bai, J., and Van Roozendael, M.: On the use of the MAX-DOAS technique for the validation of tropospheric NO$_2$ column measurements from satellite, Proc. Eumetsat Conf., 2008. 2321, 2339

Platt, U. and Stutz, J.: Differential Optical Absorption Spectroscopy, Springer-Verlag Berlin

25 Heidelberg, 2008. 2320

Richter, A., Burrows, J. P., Nuess, H., Ganier, C., and Niemeier, U.: Increase in tropospheric nitrogen dioxide over China observed from space, Nature, 437, 129–132, 2005. 2319

Sinreich, R., Friess, U., Wagner, T., and Platt, U.: Multi axis differential optical absorption spectroscopy (MAX-DOAS) of gas and aerosol distributions, Faraday Discuss., 130, 153–

30 164, 2005. 2320, 2322, 2323

Stammes, P.: Spectral radiance modeling in the UV-visible range, IRS2000: Current problems in atmospheric radiation, Eds. W.L. Smith and Y.M. Timofeyev, A. Deepak Publ., Hampton (VA), 1, 385–388, 2001. 2329

Title Page

Abstract | Introduction

Conclusions | References

Tables | Figures

|◄ | ►|

◄ | ►

Back | Close

Full Screen / Esc

Printer-friendly Version

Interactive Discussion

Stammes, P., de Haan, J. F., and Hovenier, J. W.: The polarized internal radiation field of a planetary atmosphere, Astron. Astrophys., 225, 239–259, 1989. 2329

van der A, R. J., Peters, D. H. M. U., Eskes, H., Boersma, K. F., Van Roozendael, M., DeSmedt, I., and Helder, H. M.: Detection of the trend and seasonal variation in tropospheric NO_2 over China, J. Geophys. Res., 111, D12317, doi:10.1029/2005JD006594, 2006. 2319

Vandaele, A. C., Hermans, C., Simon, P. C., Carleer, M., Colin, R., Fally, S., Merienne, M. F., Jenouvrier, A., and Coquart, B.: Measurements of the NO2 Absorption Cross-section from $42\,000\,cm^{-1}$ to $10\,000\,cm^{-1}$ (238–1000 nm) at $220\,K$ and $298\,K$, J. Quant. Spectr.Radiat. Transfer, 59, 171–184, 1997. 2326

Wagner, T., Dix, B., von Friedeburg, C., Friess, U., Sanghavi, S., Sinreich, R., and Platt, U.: MAX-DOAS O4 measurements: A new technique to derive information on atmospheric aerosols - Principles and information content, J. Geophys. Res., 109, D22205, doi: 10.1029/2004JD004904, 2004. 2320, 2322

Wagner, T., Burrows, J. P., Deutschmann, T., Dix, B., von Friedeburg, C., Frieß, U., Hendrick, F., Heue, K.-P., Irie, H., Iwabuchi, H., Kanaya, Y., Keller, J., McLinden, C. A., Oetjen, H., Palazzi, E., Petritoli, A., Platt, U., Postylyakov, O., Pukite, J., Richter, A., van Roozendael, M., Rozanov, A., Rozanov, V., Sinreich, R., Sanghavi, S., and Wittrock, F.: Comparison of box-air-mass-factors and radiances for Multiple-Axis Differential Optical Absorption Spectroscopy (MAX-DOAS) geometries calculated from different UV/visible radiative transfer models, Atmos. Chem. Phys., 7, 1809–1833, doi:10.5194/acp-7-1809-2007, 2007. 2329, 2334

Wagner, T., Ibrahim, O., Shaiganfar, R., and Platt, U.: Mobile MAX-DOAS observations of tropospheric trace gases, Atmos. Meas. Tech., 3, 129–140, doi:10.5194/amt-3-129-2010, 2010. 2322

Wittrock, F., Oetjen, H., Richter, A., Fietkau, S., Medeke, T., Rozanov, A., and Burrows, J. P.: MAX-DOAS measurements of atmospheric trace gases in Ny-Ålesund – Radiative transfer studies and their application, Atmos. Chem. Phys., 4, 955–966, doi:10.5194/acp-4-955-2004, 2004. 2320, 2321, 2334, 2336, 2339

Zhou, Y., Brunner, D., Boersma, K. F., Dirksen, R., and Wang, P.: An improved tropospheric NO_2 retrieval for OMI observations in the vicinity of mountainous terrain, Atmos. Meas. Tech., 2, 401–416, doi:10.5194/amt-2-401-2009, 2009. 2319

MAX-DOAS aerosol corrected tropospheric NO$_2$ columns

T. Vlemmix et al.

Title Page

Abstract | Introduction

Conclusions | References

Tables | Figures

◄◄ | ►►

◄ | ►
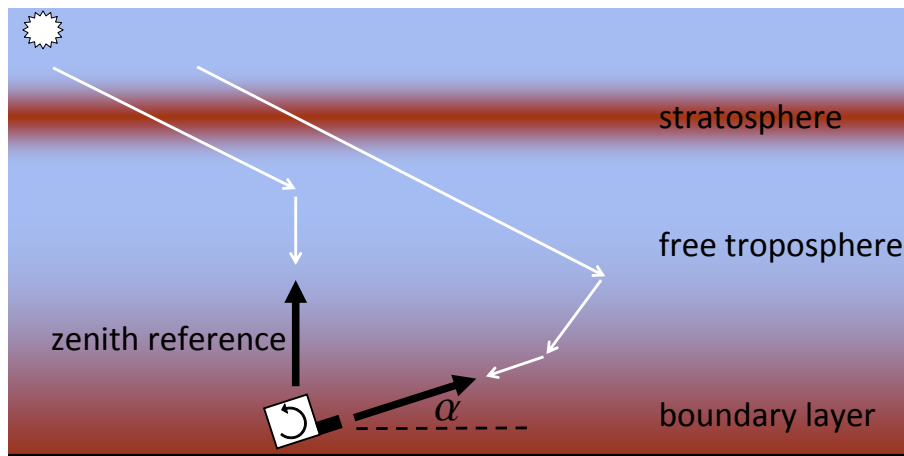
Back | Close

Full Screen / Esc

Printer-friendly Version

Interactive Discussion

Table 1. Sensitivity study of six parameters affecting relative intensity and the tropospheric NO$_2$ differential air mass factor (see Sect. 3.2): aerosol optical thickness (AOT), boundary layer height for NO$_2$ and aerosols (BLH), boundary layer column of NO$_2$ (N), asymmetry parameter of aerosols (ASY), single scattering albedo of aerosols (SSA), surface albedo (ALB), and polarization (POL). Each parameter was changed in the DAK model from case 1 (reference value) to case 2, with all other parameters unchanged. For the elevations 4°, 8° and 16°, the effect of this change in percent is given for the relative intensity (I^{rel}), for the differential air mass factor (ΔM) and for the differential air mass factor calculated by the two-step algorithm (ΔM^{alg}). The percentage was calculated as follows: $[P(\text{case 1})-P(\text{case 2})]/P(\text{case 2})\times 100\%$, where $P(\text{case 2})$ is the model simulation of quantity P for parameter setting case 2. Values were calculated for a solar zenith angle of 60° and a relative azimuth of 180°.

param.	case 1	case 2	$\alpha=4°$ change (%) in: I^{rel}	ΔM	N_α^{Tr}	$\alpha=8°$ change (%) in: I^{rel}	ΔM	N_α^{Tr}	$\alpha=16°$ change (%) in: I^{rel}	ΔM	N_α^{Tr}
AOT	0.2	0.4	54	55	0	60	29	0	40	7.4	0
BLH aer.&NO$_2$ [km]	1.0	1.5	−6.5	6.1	−11	−3.2	4.2	−4.7	−1.1	1.9	−1.6
BLH NO$_2$ [km]	1.0	1.5	−1.3	23	−24	−0.6	12	−12	−0.1	5.1	−4.7
N [10^{15} molec/cm^2]	20	2	−5.7	0.1	−3.9	−4.3	−2.7	1.8	−2.4	−7.7	7.8
ASY	0.70	0.75	−4.8	−3.7	0.15	−5.0	−3.0	1.6	−4.1	−3.1	2.8
SSA	0.92	0.95	−2.1	−0.2	−1.4	−1.2	0.1	−0.5	−0.4	−0.6	0.6
ALB	0.06	0.03	2.7	−0.5	−3.1	1.5	0.1	−0.7	0.7	0.2	−0.7
POL	on	off	2.4	0.5	1.9	2.7	0.4	0.9	−2.1	−0.4	0.0

Table 2. Comparison between OMI and MAX-DOAS tropospheric NO$_2$. The three rows represent three different sets of selection criteria that are applied to the ground-based retrieved tropospheric NO$_2$ columns. Each set consists of an upper limit of the relative measurement uncertainty (ε_{MD}^{rel} in percent) and an upper limit of the absolute measurement uncertainty (ε_{MD}^{abs} in 10^{15} molec/cm^2). A point is selected if it satisfies one or both of the limits. The other columns are: number of collocations that satisfies these criteria (n), correlation (R), mean difference ($< d >$ in 10^{15} molec/cm^2), standard deviation of differences ($\sigma_{<d>}$) in 10^{15} molec/cm^2, slope (s_{fit}) of linear fit that minimizes the sum of the squared orthogonal distances, y-axis offset of this linear fit (o_{fit} in 10^{15} molec/cm^2), mean relative and absolute measurement uncertainty of the ground based observations ($< \varepsilon_{MD}^{rel} >$ in percent and $< \varepsilon_{MD}^{abs} >$ in 10^{15} molec/cm^2), and the same quantities for the satellite observation: ($< \varepsilon_{OMI}^{rel} >$ and $< \varepsilon_{OMI}^{abs} >$).

Selection criteria			Comparison OMI – MAX-DOAS								
set	ε_{MD}^{rel}	ε_{MD}^{abs}	n	R	$< d >$	$\sigma_{<d>}$	s_{fit}	o_{fit}	$< \varepsilon_{MD}^{rel} >$	$< \varepsilon_{MD}^{abs} >$	$< \varepsilon_{OMI}^{rel} >$	$< \varepsilon_{OMI}^{abs} >$
1	$\leq 30\%$	≤ 3	76	0.64	−2.1	7.6	1.21	−0.5	23%	2.8	59%	6.3
2	$\leq 20\%$	≤ 2	48	0.73	−1.0	6.2	1.0	1.2	20%	2.0	60%	6.8
3	$\leq 10\%$	≤ 1	17	0.88	0.6	3.9	0.8	1.2	22%	0.9	57%	6.4

stratosphere

free troposphere

zenith reference

α

boundary layer

Fig. 1. Illustration of MAX-DOAS observation. The Mini MAX-DOAS instrument of this study can rotate only in one vertical plane, i.e. it has a fixed azimuth. The viewing direction is referred to as the elevation, which is the angle (α) with the horizontal. For both the DOAS method and relative intensity observations, an observation at elevation α is always combined with a zenith observation ($\alpha = 90°$). Two examples of photon paths are shown in white. MAX-DOAS observations are relatively insensitive to the trace gases in the stratosphere, as long as the zenith and non-zenith observations are taken within a time frame where the solar zenith angle changes only little: the sensitivity of the MAX-DOAS observation to NO_2 in a particular horizontal layer is proportional to the difference in (detected) photon path length through that layer, between the observations pointed at the zenith and at elevation α.
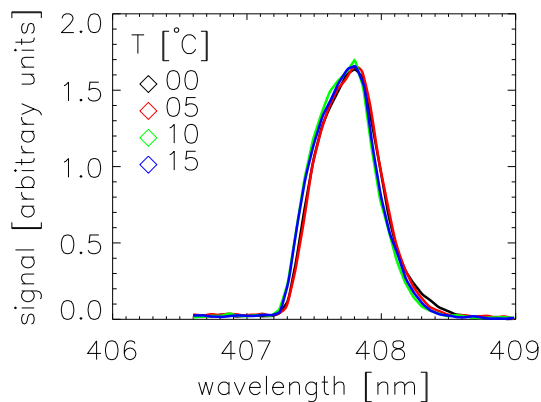
Fig. 2. Measurements with the Mini MAX-DOAS instrument of a Mercury line source at 407.8 [nm], at four different temperatures.
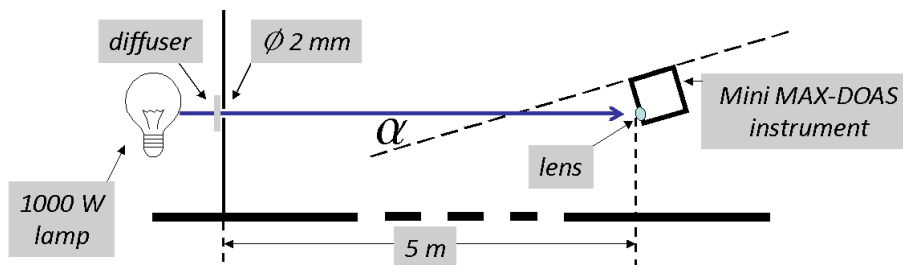
Fig. 3. Set-up of the field-of-view characterization experiment with a light source in the distance. The angle α denotes the rotation in the vertical plane relative to a horizontal starting position of 0°. At this starting position the light source was at the same height above the table as the lens. The experiment was repeated including a black tube in front of the lens (not drawn), which is used normally to block stray light. Adding the tube did not change the results.
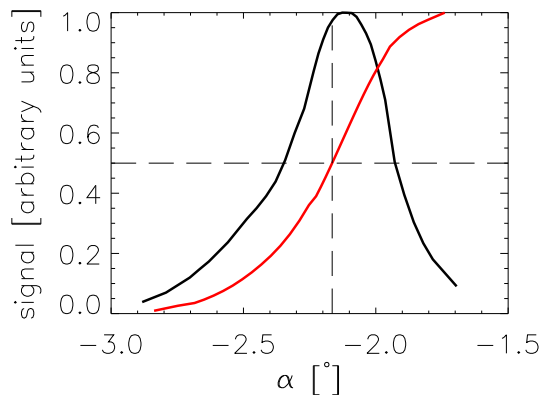
Fig. 4. Field-of-view of the Mini MAX-DOAS instrument, measured with the set-up of Fig. 3. The black curve represents the measured signal at elevation α, and the red curve is the normalized surface integral of the black curve. The FWHM is 0.4°. The center of the field-of-view is defined as the elevation where the red curve equals one half. In this case the pointing offset is −2.16°.
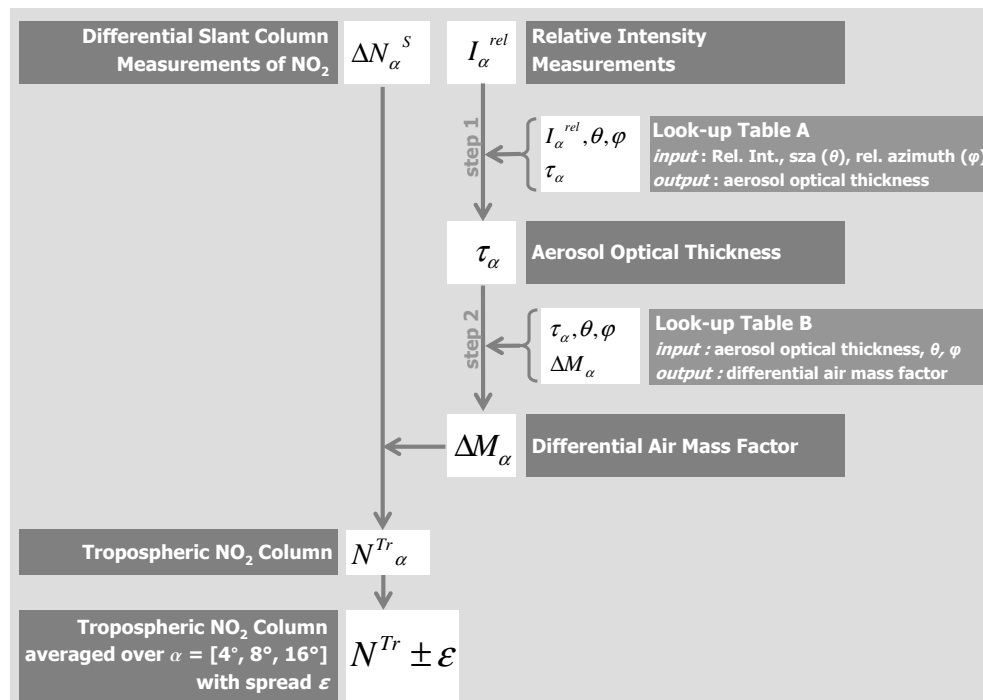
Fig. 5. Flow chart of the two-step retrieval algorithm of tropospheric NO$_2$ columns.

Full Screen / Esc
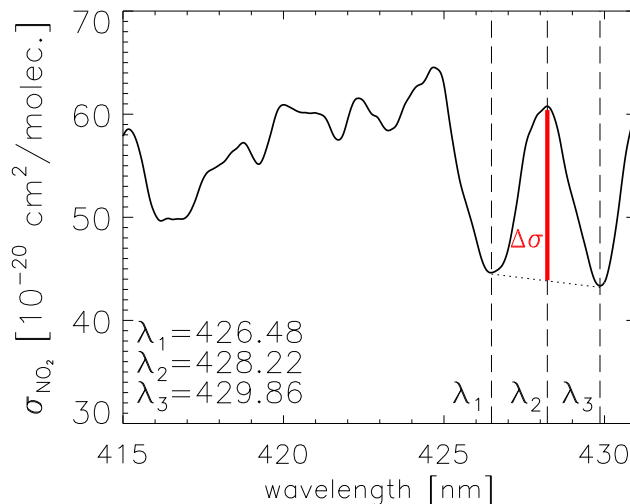
Fig. 6. Spectrum of the NO$_2$ absorption cross-section convoluted with the instrumental slit function. The three wavelengths λ_1, λ_2 and λ_3 were used in the radiative transfer simulation of the differential AMF and relative intensity. The wavelength range of this figure corresponds to the DOAS spectral fitting window (see Sect. 2.3.2).
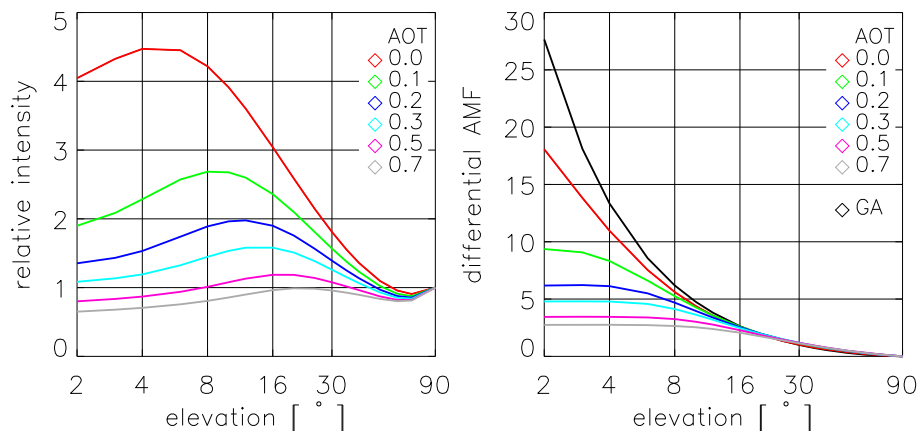
Fig. 7. Radiative transfer simulations with the DAK model of relative intensity (left) and the differential air mass factor of NO$_2$ (right) at 428.22 nm as a function of the elevation, for different values of the AOT. Note the logarithmic scale on the x-axis. The black line in the right plot gives the differential air mass factor for the geometrical approximation (GA). Solar zenith angle = 50°, relative azimuth angle = 180°.
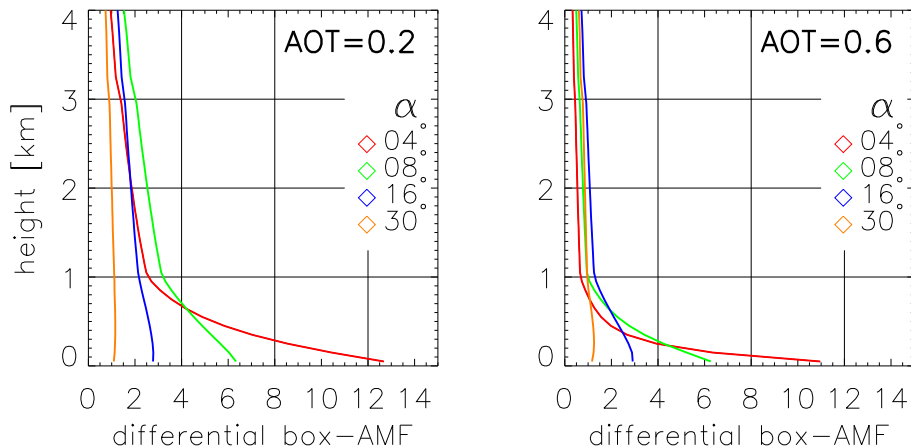
Fig. 8. Radiative transfer simulations with the DAK model of height-dependent differential AMF (differential box-AMF) for AOT=0.2 (left) and AOT=0.6 (right), at 428.22 nm. Settings in the simulations: boundary layer height for aerosols (block profile): 1.0 km, solar zenith angle = 60°, relative azimuth angle = 180°, λ=428 nm.
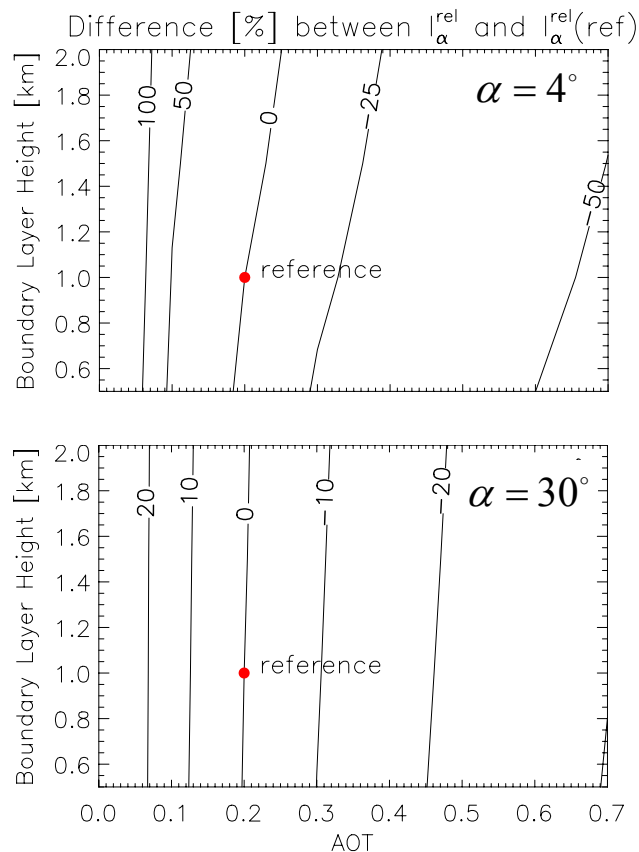
Fig. 9. Difference between the modeled relative intensity for a range of AOT and BLH values, and the reference value of relative intensity for AOT=0.2 and a boundary layer height of 1 km (red dot). Two elevations were used in the calculations: 4° (top) and 30° (bottom). Solar zenith angle = 50°, relative azimuth angle = 180°, λ=428 nm.

Title Page

Abstract | Introduction

Conclusions | References

Tables | Figures

|◄ | ►|

◄ | ►

Back | Close

Full Screen / Esc

Printer-friendly Version

Interactive Discussion
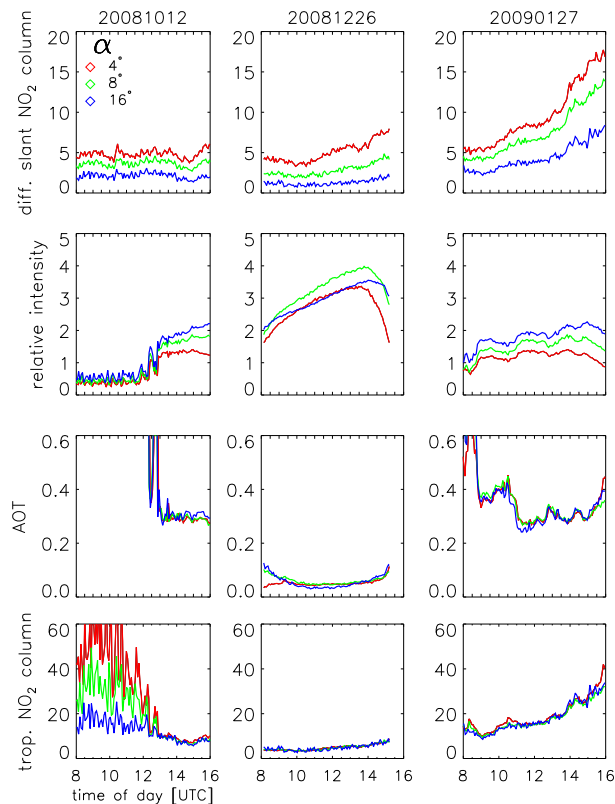
Fig. 10. Tropospheric NO$_2$ column retrieval for three selected days using the two-step algorithm. All plots have the same time scale on the horizontal axis and in each plot the colors correspond to the elevations indicated by the legend on the upper left. The first row shows the measured NO$_2$ differential slant columns in [10^{16} molecules/cm^2]. The second row shows the relative intensities, and the third row the retrieved AOT. The last row shows the retrieved tropospheric column of NO$_2$ in [10^{15} molecules/cm^2].

Title Page

Abstract | Introduction

Conclusions | References

Tables | Figures

◄ | ►|

◄ | ►

Back | Close

Full Screen / Esc

Printer-friendly Version

Interactive Discussion
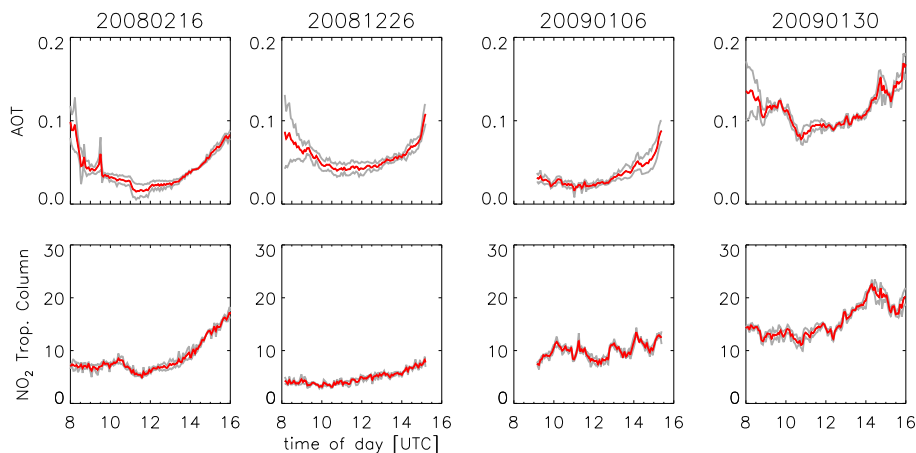
Fig. 11. Retrieved aerosol optical thickness (upper row) and tropospheric NO_2 column (lower row) for four selected days using the two-step algorithm. The red lines represent the average value of the three elevations: 4°, 8°, and 16°. The spread is indicated by the grey lines.

Title Page

Abstract | Introduction

Conclusions | References

Tables | Figures

|◄ | ►|

◄ | ►

Back | Close

Full Screen / Esc

Printer-friendly Version

Interactive Discussion
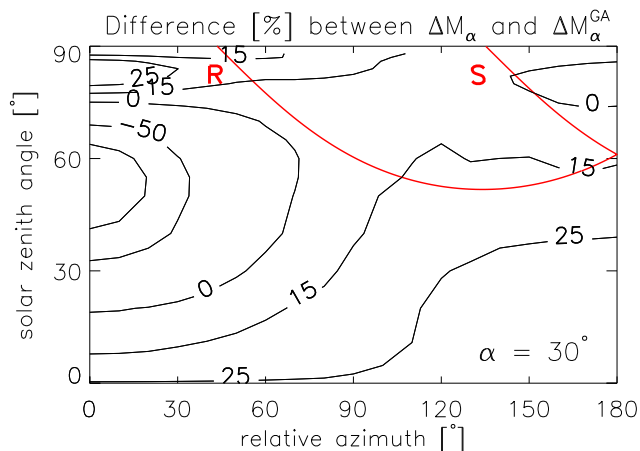
Fig. 12. Difference between the differential air mass factor simulated with the DAK radiative transfer model, and the differential air mass factor of the geometrical approximation (GA) for 30° elevation, as a function of solar position. AOT = 0.2, λ = 428.22 nm. As an example, the red curve represents the path of the sun trough the sky above De Bilt on 21 March 2009, relative to the viewing azimuth of the instrument, which was 46° East from North (sunrise is indicated by "R", sunset by "S").

Title Page

Abstract | Introduction

Conclusions | References

Tables | Figures

|◄ | ►|

◄ | ►

Back | Close

Full Screen / Esc

Printer-friendly Version

Interactive Discussion
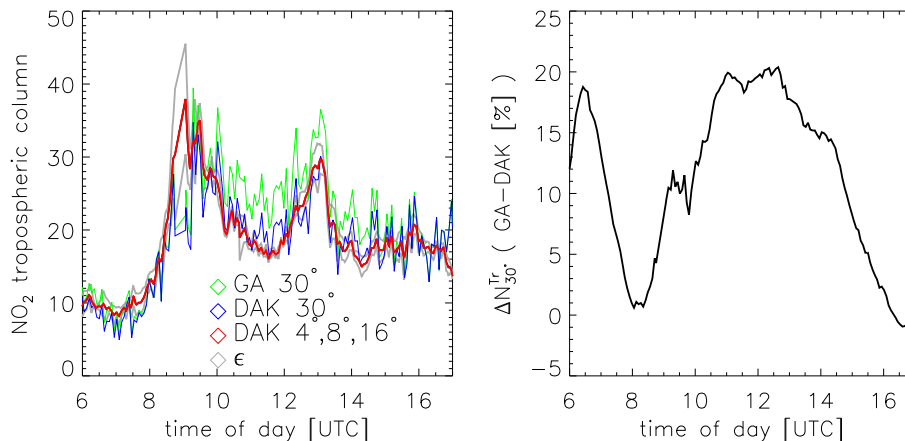
Fig. 13. Retrieved tropospheric NO$_2$ column in units of [10^{15} molec/cm^2] for 21 March 2009 (left graph). The different colors represent variations of the retrieval method. The green line is based on the geometrical approximation (GA), applied to the differential slant column measurements at 30° elevation. The blue line is derived from the same measurements, but with a differential air mass factor calculated with the DAK model and the settings described in Sect. 3.1.2, where the AOT was derived from the relative intensity measurements at this elevation. The red line is the average tropospheric column as derived by the two-step algorithm, i.e. from the elevations 4°, 8° and 16°. The spread in these values is shown in grey. The noisy character of the retrievals based on the 30° elevation is due to the low sensitivity to NO$_2$ at 30°, relative to the other elevations. The right graph gives the difference in percent between the blue and the green line. See also the red line in Fig. 12.

N=1251
R=0.85
$\langle X{-}Y \rangle = 0.01 +/- 0.08$
$Y = 1.01X - 0.01$

AOT (MAX−DOAS)

AOT (AERONET)
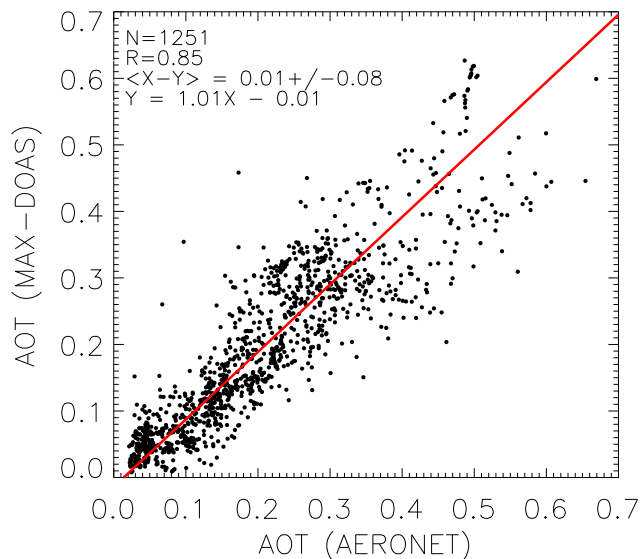
Fig. 14. Comparison between AOT derived from MAX-DOAS relative intensity observations in De Bilt and AERONET AOT (Cabauw). Both sites were 22 km apart. The selection criteria described in Sect. 4.3 were applied to all measurements in the observation period (see Sect. 2.2). The red line represents a linear regression, where the squared orthogonal distance of all points to the 1:1 line was minimized.

Title Page

Abstract | Introduction

Conclusions | References

Tables | Figures

|◄ | ►|

◄ | ►

Back | Close

Full Screen / Esc

Printer-friendly Version

Interactive Discussion
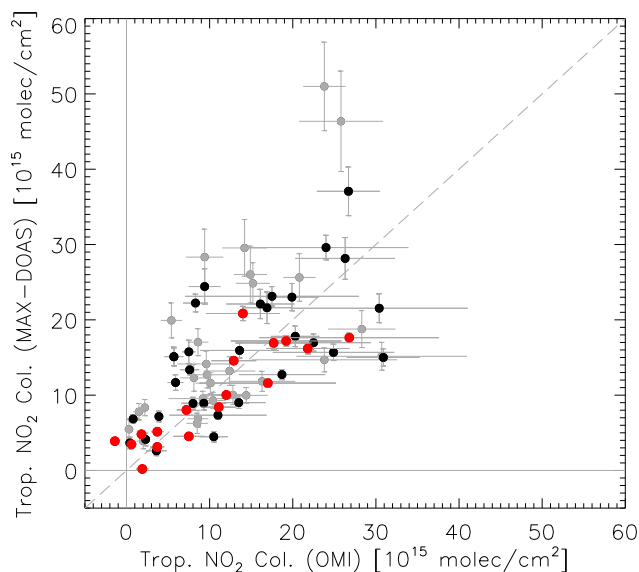
Fig. 15. Comparison between tropospheric NO$_2$ columns from MAX-DOAS observations in De Bilt and OMI (DOMINO product). The selection of data-points is described in Table 2 (MAX-DOAS), and Sect. 4.4 (OMI), and was applied to all measurements in the observation period (see Sect. 2.2). The selection described in the first row of Table 2 includes all points in the plot, the selection described in the second row includes all black and red points, and the selection of the last row includes only the red points.